

# Diverse Responses to Vascular Disrupting Agent Combretastatin A4 Phosphate: A Comparative Study in Rats with Hepatic and Subcutaneous Tumor Allografts Using MRI Biomarkers, Microangiography, and Histopathology<sup>1</sup>

Junjie Li<sup>\*,†</sup>, Feng Chen<sup>\*,†</sup>, Yuanbo Feng<sup>\*,†</sup>,  
Marlein Miranda Cona<sup>\*,†</sup>, Jie Yu<sup>\*</sup>,  
Alfons Verbruggen<sup>‡</sup>, Jian Zhang<sup>§</sup>,  
Raymond Oyen<sup>\*</sup> and Yicheng Ni<sup>\*,†,§</sup>

<sup>\*</sup>Theragnostic Laboratory, Department of Imaging and Pathology, Biomedical Sciences Group, KU Leuven, Leuven, Belgium; <sup>†</sup>Molecular Small Animal Imaging Centre (MoSAIC), Biomedical Sciences Group, KU Leuven, Leuven, Belgium; <sup>‡</sup>Faculty of Pharmaceutical Sciences, KU Leuven, Leuven, Belgium; <sup>§</sup>Laboratory of Translational Medicine, Jiangsu Academy of Traditional Chinese Medicine, Nanjing, Jiangsu Province, China

## Abstract

**OBJECTIVE:** Differently located tumors of the same origin may exhibit diverse responses to the same therapeutics. To test this hypothesis, we compared the responses of rodent hepatic and subcutaneous engrafts of rhabdomyosarcoma-1 (R1) to a vascular disrupting agent Combretastatin A4 phosphate (CA4P). **METHODS:** Twelve WAG/Rij rats, each bearing three R1 implanted in the right and left hepatic lobes and subcutaneously in the thoracic region, received CA4P intravenously at 5 mg/kg ( $n = 6$ ) or solvent ( $n = 6$ ). Therapeutic responses were compared interindividually and intraindividually among tumors of different sites till 48 hours after injection using *in vivo* MRI, postmortem digital microangiography, and histopathology. **RESULTS:** MRI revealed that the subcutaneous tumors (STs) significantly increased in volume than hepatic tumors (HTs) 48 hours after CA4P ( $P < .05$ ). Relative to vehicle controls and treated group at baseline, necrosis ratio, apparent diffusion coefficient, and enhancement ratio changed slightly with the STs but significantly with HTs ( $P < .05$ ) after CA4P treatment. Vessel density derived from microangiography was significantly lower in STs compared to HTs without CA4P treatment. CA4P treatment resulted in decreased vessel density in HTs, while it did not affect vessel density in STs. MRI and microangiography outcomes were supported by histopathologic findings. **CONCLUSIONS:** MRI and microangiography allowed quantitative comparison of therapeutic responses to CA4P in rats with multifocal tumors. The discovered diverse effects of the same drug on tumors of the same origin but different locations emphasize the presence of cancer heterogeneity and the importance of individualization of drug delivery.

*Translational Oncology* (2013) 6, 42–50

Address all correspondence to: Prof. Yicheng Ni, Theragnostic Laboratory, Department of Imaging and Pathology, Biomedical Sciences Group, KU Leuven, Herestraat 49, BE-3000 Leuven, Belgium. E-mail: Yicheng.ni@med.kuleuven.be

<sup>1</sup>This work was partially supported by grants awarded by FWO Vlaanderen ZWAP/05/018; Geconcerteerde Onderzoeksactie of the Flemish Government, OT Project (OT/06/70); the KU Leuven Molecular Small Animal Imaging Centre (MoSAIC; KUL EF/05/08); the Center of Excellence *In Vivo* Molecular Imaging Research (IMIR) of KU Leuven; the IWT SBO "Imagine" (SBO80017); the National Natural Science Foundation of China (81071828); Jiangsu Province Natural Science Foundation (BK2010594); and EU Project Asia-Link CFP 2006-EuropeAid/123738/C/ACT/Multi-Proposal No. 128-498/111. The corresponding author (Y.N.) is currently a Bayer Lecture Chair Holder. All authors declare no conflict of interest regarding the content of the paper.

Received 27 October 2012; Revised 25 December 2012; Accepted 31 December 2012

## Introduction

Cancer is a largely unpredictable phenomenon involving complex interactions between various processes and factors in malignant cells and their microenvironment. Such complexities may result in markedly different responses to a given treatment. The tumor vasculature is an attractive target for therapy, because most tumor cells rely on an intact vascular supply for their survival and growth. Vascular disrupting agents (VDAs) that specifically target the endothelia, pericytes, or specific proteins derived from the tumoral endothelium represent a fundamentally new cancer-targeting strategy. Upon systemic administration of VDAs that destroy the abnormal irregularly structured tumoral vasculature, cancer cells are deprived of blood, oxygen, and nutrient supply, leading to intratumoral hemorrhagic necrosis [1–3].

Combretastatin A4 phosphate (CA4P) is a small molecular VDA that has been most intensively studied in preclinical research and clinical trials [4–7]. It is the water-soluble phosphate prodrug of Combretastatin A4, which is originally extracted from South African willow tree, *Combretum caffrum* [8,9]. Following intracellular uptake, CA4P is *in vivo* dephosphorylated by nonspecific endogenous phosphatases into the active form of Combretastatin A4, the latter then binds to the colchicines-binding site in  $\beta$ -tubulin of microtubule [10]. Although structurally similar to colchicines, CA4P binds to tubulin more rapidly with greater affinity comparing to colchicines [10,11]. An immediate vascular collapse can be induced following injection of CA4P at a dose of one tenth the maximum tolerated dose in experimental tumors [12], which consequently causes delay of tumor growth [8,13–16]. Extensive central necrosis up to 90% of tumor mass occurs with a thin rim of viable tumor tissue fed by peripheral normal vessels [17,18]. This remaining viable tissue is responsible for the rapid tumor regrowth after a single administration found in preclinical models [19]. Therefore, practically CA4P often has to combine with cytotoxic agents, radiotherapy, and angiogenesis inhibitors to achieve enhanced tumor control [20–24].

Proper understanding of tumor responses to CA4P may provide new avenues for overcoming drug resistance and improving therapeutic efficacy [25]. The susceptibility of different tumor types to CA4P has been studied extensively [26–30]. However, previous studies on CA4P were performed in animal models with tumor growing either in one certain viscus [24,30,31] or in subcutaneous lacuna [32–34]. We hypothesized that tumors of the same nature but in different organs may reveal different therapeutic responses to the same anticancer agent. To the best of our knowledge, such an intraindividual comparison of tumor responses to CA4P has never been experimentally investigated.

To verify our hypothesis, we developed a rat model of multifocal tumors, i.e., two hepatic tumors (HTs) and one subcutaneous tumor (ST), by surgical implantation of rhabdomyosarcoma-1 (R1) tissues. Tumor responses to CA4P and vehicle were compared interindividually and intraindividually among tumors in different sites using *in vivo* magnetic resonance imaging (MRI) biomarkers and postmortem digital microangiography and histopathology.

## Materials and Methods

### Tumor Models

This animal study was in compliance with national and European regulations and approved by the Institutional Ethical Committee for Animal Care and Use. Twelve male WAG/Rij rats weighting around 240 to 270 g received R1 tumors engrafted in the left and right hepatic lobes and at subcutaneous thorax [20,35]. Briefly, animals underwent

midline laparotomy after being anesthetized with intraperitoneal injection of pentobarbital (Nembutal; Sanofi Sante Animale, Brussels, Belgium) at 50 mg/kg. Three freshly harvested R1 tissue cubes of approximately 2 mm<sup>3</sup> from a tumor-bearing donor rat were implanted into the left and right hepatic lobes as well as subcutaneous thorax to produce trifocal models, i.e., two HTs and one ST in each rat. Tumor growth was followed with MRI every 2 days from 1 week after the implantation.

### Experimental Protocol

The experiment began when tumors reached a diameter of 0.7 to 1.2 mm at 14 days after implantation. These rats received either intravenous (iv) injection of CA4P at a dose of 5 mg/kg ( $n = 6$ ) or equal volume of the solvent as vehicle controls ( $n = 6$ ). All rats were *in vivo* examined by MRI at 30 minutes before and 4, 24, and 48 hours after the injection. Rats were killed immediately after the last MRI session for postmortem microangiography and histopathology (Figure 1). The derived parameters reflecting therapeutic responses were compared interindividually and intraindividually among tumors at different time points.

### Magnetic Resonance Imaging

A clinical 1.5-T whole-body MRI magnet (Symphony; Siemens, Erlangen, Germany) with a maximum gradient capability of 30 mT/m was used. Scanning was performed using a four-channel phased array human wrist coil (MRI Devices, Waukesha, WI). As described elsewhere [31], the rat was gas-anesthetized using a mask connected via a polyethylene tube to a Harvard Apparatus System (Holliston, MA) outside the MRI suite. During imaging, the anesthesia was maintained with inhalation of 2% isoflurane in the mixture of 20% oxygen and 80% room air. The rat was placed supinely in a plastic holder inside the coil with the penile vein cannulated for contrast agent and drug administration.

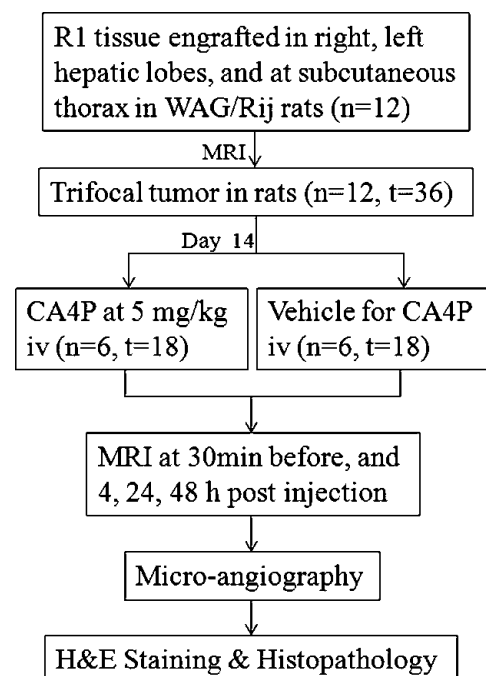


**Figure 1.** Flow chart of experimental protocol;  $n$ , number of animals;  $t$ , number of tumors.

After axial, coronal, and sagittal scout images for localization, T2-weighted imaging (T2WI), T1-weighted imaging (T1WI), diffusion-weighted imaging (DWI), and contrast-enhanced T1WI (CE-T1WI) were acquired in a transverse plane in all rats with slice thickness of 2.0 mm and a gap of 0.4 mm. For the DWI, diffusion gradients were applied with 10 different  $b$  values (0, 50, 100, 150, 200, 250, 300, 500, 750, and 1000 s/mm<sup>2</sup>) in three dimensions ( $x$ ,  $y$ , and  $z$ ) and averaged for the calculation of the isotropic apparent diffusion coefficient (ADC) values. A parallel imaging technique was applied with an acceleration factor of 2 to reduce susceptibility artifacts and examination times [24]. For CE-T1WI, gadolinium-based contrast agent Gd-DOTA (Dotarem, Guerbet, France) at a dose of 0.2 mmol/kg was administered 1 minute in advance. The acquisition parameters for all imaging sequences are given in Table 1.

### MRI Analyses

Image analyses were conducted using the built-in software on the Siemens workstation to obtain the following measurements. All measurable parameters were acquired by the three authors with consensus.

**Tumor volume.** T1WI, T2WI, and CE-T1WI were used as the routine sequences to determine the tumor volume, location, and area of necrosis. Tumor area was contoured manually on each slice of T2WI. Tumor volume was calculated using the equation: tumor volume =  $\sum$ [tumor area on each slice  $\times$  (slice thickness + gap)]. Tumor volume doubling time (DT) was calculated as described elsewhere [36] using the following equation:  $DT = (t_2 - t_1) \times \ln 2 / \ln (V_2/V_1)$ , where  $t_2 - t_1$  indicates the length of time between two measurements, and  $V_2$  and  $V_1$  denote the tumor volume measured at two points.

**Tumor necrosis ratio.** Central nonenhancing area on CE-T1WI is considered necrosis. Necrosis volume was calculated the same way as tumor volume. Necrosis ratio was defined as the volume of necrosis over that of the entire tumor volume.

**Calculation of ADC and normalization of signal intensity.** ADC values were calculated from DWI by using the following monoexponential equation:  $S_i = S_0 \exp(-b_i \text{ADC})$  [29,37], where  $S_i$  is the signal intensity (SI) measured on the  $i$ th  $b$  value image,  $b_i$  is the corresponding  $b$  value, and  $S_0$  is a variable that estimates the intrinsic SI (for  $b = 0$  s/mm<sup>2</sup>). The percentile change in ADC at different time points after treatment was defined by the equation  $(\text{ADC}_{\text{post}} - \text{ADC}_{\text{baseline}}) / \text{ADC}_{\text{baseline}} \times 100$  to quantify therapy-related changes.

The measured SI was corrected with the phantoms from baseline images as a standard reference. A region of interest (ROI) of 200 pixels was placed on each phantom, and the SIs derived from two phantoms were averaged as a standard value. The following formula was used to normalize SI of each image:  $\text{SI}_{\text{corrected}} = \text{SI}_{\text{measured}} \times (\text{SI}_{\text{phantom measured}} / \text{SI}_{\text{phantom standard}})$ . By comparing to the liver parenchyma, the SI of tumor was defined as hypointense, isointense, or hyperintense.

**Tumor enhancement ratio.** The tumor was delineated with an operator-defined ROI on three central tumor-containing image slices, and the average tumor SI was automatically generated on CE-T1WIs. Enhancement ratio (ER) of SI was calculated to compare the degrees of SI enhancement at different time points after the injection of Gd-DOTA. The following formula was used:  $\text{ER} = (\text{SI}_{\text{postCA4P}} - \text{SI}_{\text{baseline}}) / \text{SI}_{\text{baseline}} \times 100\%$ , where ER is the enhancement ratio between the SI enhancement

**Table 1.** Parameters for MRI Sequences.

	T1WI	T2WI	DWI	CE-T1WI
Sequence type	TSE	TSE	EPI	TSE
Repetition time	535	3810	1900	535
Echo time	9.2	106	95	9.2
Flip angle (degrees)	180	160	—	180
Turbo/EPI factor	7	19	91	7
Field of view (mm <sup>2</sup> )	50 $\times$ 140	50 $\times$ 140	58.3 $\times$ 162	50 $\times$ 140
Imaging acquisition matrix	100 $\times$ 256	100 $\times$ 256	81 $\times$ 192	100 $\times$ 256
In-plane resolution (mm <sup>2</sup> )	0.5 $\times$ 0.5	0.5 $\times$ 0.5	1.0 $\times$ 0.8	0.5 $\times$ 0.5
Slice thickness (mm)	2	2	2.4	2
Number of averages	4	3	6	4
Total acquisition time(s)	84	85	326	84

TSE, turbo spin echo; EPI, echo-planar imaging.

post-CA4P relative to that at the baseline, and  $\text{SI}_{\text{postCA4P}}$  and  $\text{SI}_{\text{baseline}}$  are the SIs measured on post-CA4P and baseline CE-T1WIs, respectively.

### Digital Microangiography and Vessel Density Quantification

Immediately after MRI sessions, rats were first heparinized with an iv bolus of 500 U/kg and then killed with an overdose of pentobarbital intraperitoneally. With a neck skin incision, the right carotid artery and jugular vein were cannulated and the blood pool was flushed with 50 ml of 5% glucose in normal saline. Barium sulfate suspension of 10 ml was injected via the carotid catheter and the efflux was drained via jugular vein. The rats were then radiographed with a digital mammography unit (Em-brace; Agfa-Gevaert, Mortsel, Belgium) at 35 kV and 16 mAs. All tumors were then excised and fixed in 10% formalin for 48 hours. The fixed tumors were radiographed and then sliced into 3-mm sections in the plane similar to the axial MR images using a Plexiglas matrix (Agar Scientific, Essex, England), and the sections were radiographed again for quantifications of vessel density.

Digitized photographs from microangiography were analyzed using the ImageJ software for quantification of relative vessel density. Tumor areas in radiographic imaging were contoured as ROIs in all tumor-containing sections. As an index of vascular density, the mean gray values generated from the ImageJ software were compared between HTs and STs from CA4P-treated rats and from vehicle controls as reference.

### Hematoxylin and Eosin Staining and Histopathology

After microangiography, all tumor sections were paraffin embedded and sliced into 10  $\mu$ m using a microtome. The slides were then stained with hematoxylin and eosin (H&E) for microscopic assessment (Axioskop; Zeiss, Oberkochen, Germany) with  $\times 50$  to  $\times 400$  magnifications. Histologic findings were further co-localized with the corresponding MRI and microangiographic images for mutual verifications.

### Statistical Analysis

Numerical data were expressed as means  $\pm$  SD. Statistical analysis was performed using SPSS (version 18.0, Chicago, IL). Tumor volume, necrosis over tumor ratios, SIs, and vascular density among tumors in different locations were compared using one-way analysis of variance. A significant difference was considered for  $P < .05$ .

## Results

### General Aspects

All rats survived the anesthesia, tumor implantation and growth, and MRI sessions and tolerated well with iv drug administrations. Trifocal

tumors including two HTs in the right and left liver lobes and one ST at subcutaneous thorax were successfully induced in all 12 rats, resulting in a sample size of 36 R1 tumors in total.

### MRI Findings

All HTs were hypointense on T1WIs but hyperintense on T2WIs at all time points. On CE-T1WIs, all HTs appeared hyperenhanced at baseline in CA4P-treated group and at all time points in vehicle control group. R1 tumors in the left and right hepatic lobes showed almost identical MRI outlooks in the same group of rats. In all HTs of CA4P-treated group only, a central signal void was surrounded by a hyperenhanced rim on CE-T1WIs at 4 hours, and particularly at 24 and 48 hours after therapy, suggesting CA4P-induced vascular shutdown and subsequent intratumoral necrosis. However, all STs showed similar MRI behaviors in both groups, i.e., hypointense on T1WIs, hyperintense on T2WIs, and hyperenhanced on CE-T1WIs without being affected by CA4P injection (Figure 2). On DWI-derived ADC maps, all tumors appeared somewhat hyperintense at baseline. All tumors in vehicle control group showed ignorable changes within 48 hours. However, in CA4P-treated rats, the HTs revealed higher signal intensities in the central region at 4, 24, and 48 hours (Figure 2), suggesting enhanced water diffusion due to tumorolysis resulting from CA4P-induced ischemic necrosis. By contrast, the STs showed slight signal increase only at 4 hours, likely due to CA4P-induced reversible tumor tissue injury or edema that recovered spontaneously in 24 to 48 hours (Figure 2). Besides these visual findings, a number of quantitative measurable parameters including tumor volume, DT, tumor necrosis ratio, ADC, and ER were derived from

MRI to serve as imaging biomarkers for detecting therapeutic responses as detailed below.

**Tumor volume.** The corresponding tumor volume growth curves were shown in Figure 3A. Tumor volumes of the HTs and STs at baseline were  $0.84 \pm 0.41$  and  $1.08 \pm 0.43$  cm<sup>3</sup> and  $0.96 \pm 0.38$  and  $0.89 \pm 0.49$  cm<sup>3</sup> in vehicle control and CA4P-treated group, respectively, without significant differences ( $P > .05$ ). In CA4P-treated rats, the HTs presented a slower growth with the tumor volume of  $0.88 \pm 0.44$ ,  $0.95 \pm 0.41$ , and  $1.03 \pm 0.45$  cm<sup>3</sup>, in contrast to a rapid growth of STs with the tumor volume of  $1.24 \pm 0.50$ ,  $1.53 \pm 0.59$ , and  $1.78 \pm 0.66$  cm<sup>3</sup> at 4, 24, and 48 hours, respectively. Significant differences ( $P < .05$ ) were found between HTs and STs at 48 hours. However, in vehicle control rats, both HTs and STs grew steadily (Figure 3A) unlike the discrepancy seen with CA4P-treated group. Comparing to vehicle control rats, CA4P-treated rats revealed a significant decline in tumor volume growth only in the HTs ( $P < .01$ ) but not in the STs ( $P > .05$ ) within 48 hours after injection (Figure 3A), suggesting diverse responses to CA4P between the HTs and the STs.

**Tumor volume DT.** As an index for tumor growth, tumor volume DTs from baseline to 48 hours after CA4P were  $8.3 \pm 2.9$  and  $2.8 \pm 0.6$  days in HTs and STs, respectively, with a significant difference ( $P < .01$ ). Comparing to the vehicle control rats with a tumor DT of  $2.6 \pm 0.8$  and  $2.9 \pm 0.9$  days in the HTs and STs, respectively, a significant difference ( $P < .001$ ) was shown in DTs of HTs between CA4P-treated and vehicle control rats, but DTs of STs revealed no significant difference between the two groups. A distinctly prolonged

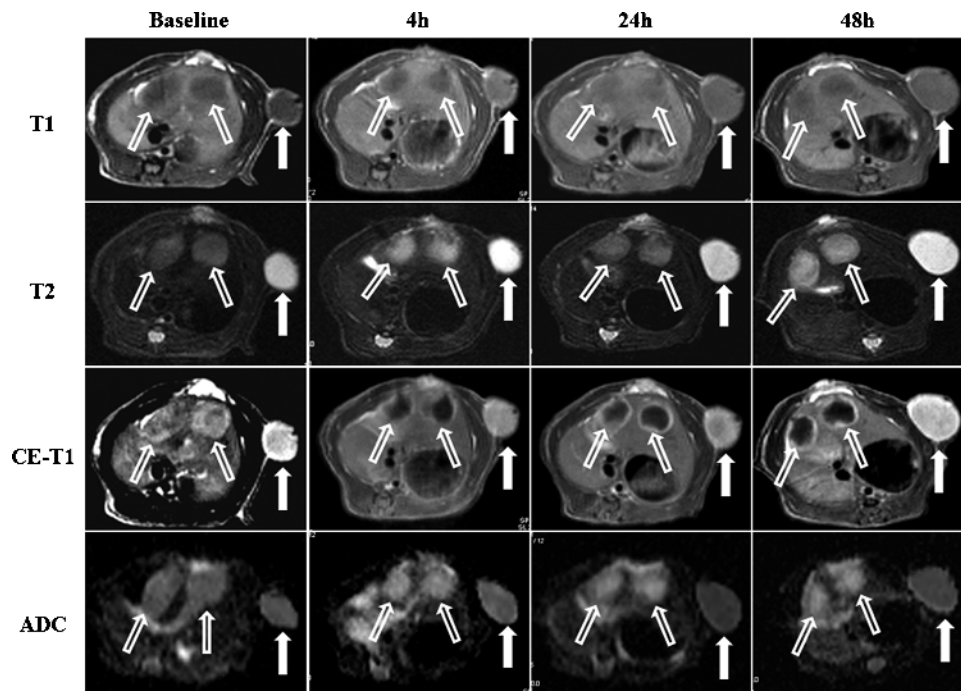


**Figure 2.** MRI findings in a rat with trifocal hepatic (HTs) and subcutaneous (ST) R1 tumors at baseline, 4, 24, and 48 hours after CA4P. Relative to liver parenchyma, at all time points, the HTs (hollow arrows) and ST (solid arrow) all appeared hypointense on precontrast T1WIs and hyperintense on T2WIs. On CE-T1WIs, although the HTs and ST were all hyperenhanced at baseline, only the ST could be entirely enhanced at 4, 24, and 48 hours, with the HTs shown as unenhanced masses surrounded by a hyperenhanced rim of SI increasing with time, suggesting the presence of CA4P-induced necrosis only in HTs but not in the ST. On DWI-derived ADC maps, all tumors shared the same SI at baseline, suggesting intact tumor viability; however, after CA4P injection, the signal became stronger only in the HTs, suggesting impaired tumor viability there but not in the ST.



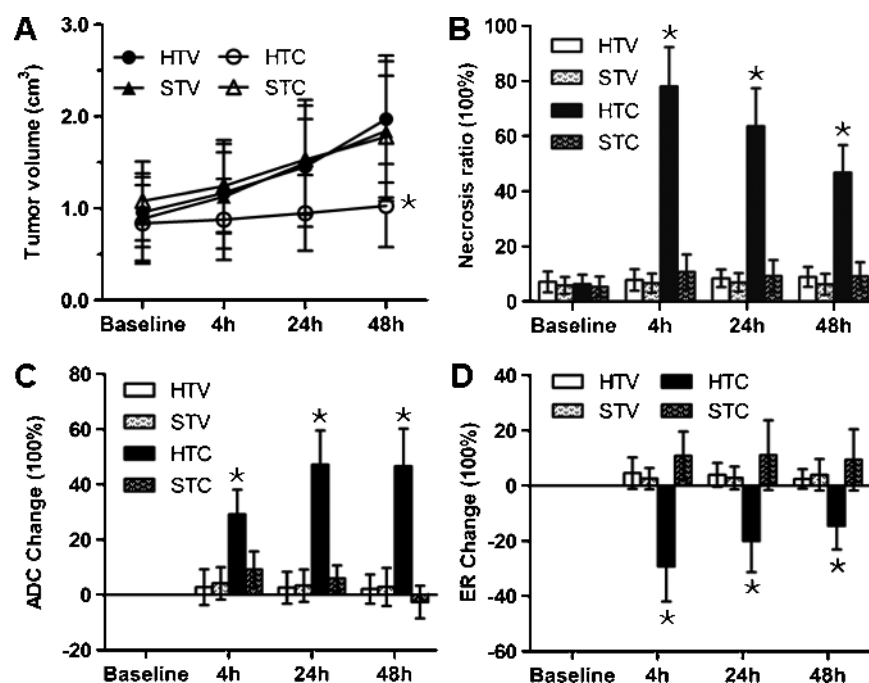


**Figure 3.** Quantitative MRI-derived biomarkers in CA4P-treated and vehicle control groups (HTV, HTs from vehicle control rats; STV, STs from vehicle control rats; HTC, HTs from CA4P-treated rats; STC, STs from CA4P-treated rats; \* $P < .05$  in comparison with STC, HTV, and STV at the same time point). (A) Line chart comparing tumor volumes at different time points. The HTs showed a delayed growth, with the tumor volume significantly smaller than the STs at 48 hours after CA4P. (B) Bar chart shows the percentile of necrosis over tumor ratios at different time points. Necrosis ratio of the HTs rose from less than 10% to about 80% at 4 hours and still remained about 50% 48 hours after CA4P. By contrast, little changes presented with the STs, similar to that of controls. (C) Bar chart of ADC percentile changes relative to the baseline value shows a drastic increase in the HTs at 4, 24, and 48 hours after CA4P, relative to the negligible changes in the STs and control animals. (D) Bar chart of percentile changes in ER relative to the baseline value derived from CE-T1WIs shows drastically decreased values only with the HTs at 4, 24, and 48 hours after CA4P, relative to the slight changes in the STs and control group.

DT indicated a much slower growth of the HTs after CA4P injection; meanwhile, the growth of STs remained unaffected by CA4P.

**Tumor necrosis ratio.** In vehicle control rats, CE-T1WI-derived necrosis ratios remained constantly minimal in both HTs and STs within 48 hours (Figure 3B). In CA4P-treated rats, tumor necrosis ratio was  $6.3 \pm 3.4\%$  and  $5.3 \pm 3.7\%$  in HTs and STs, respectively, at baseline without significant difference ( $P > .05$ ). However, relative to the little change with STs, a sharp increase of necrosis ratios to  $78 \pm 14\%$ ,  $64 \pm 14\%$ , and  $47 \pm 10\%$  at 4, 24, and 48 hours, respectively, occurred with HTs (Figure 3B) due to CA4P-induced massive intratumoral necrosis. Necrosis ratios in HTs gradually decreased with time as a result of tumor regrowth at the periphery. Significant differences ( $P < .01$ ) of necrosis ratios were found between HTs and STs at all time points after CA4P.

**Apparent diffusion coefficient.** ADC values derived from DWI served as an imaging biomarker for tissue viability assessment (Figure 3C). All tumors in vehicle control rats showed no ADC changes over 48 hours, indicating virtually intact tumor viability. In CA4P-treated rats, significant differences in ADC changes were found between HTs and STs at 4, 24, and 48 hours after CA4P ( $P < .01$ ). Comparing with vehicle control rats, ADC changes in HTs increased significantly ( $P < .001$ ) after CA4P injection.

**Enhancement ratio.** CA4P-induced vascular shutdown caused a decrease of ER in HTs but a slight increase of ER in STs, with significant

differences ( $P < .01$ ) between the HTs and STs at 4, 24, and 48 hours after CA4P injection (Figure 3D). Comparing to the HTs in vehicle control rats, the HTs in CA4P-treated rats demonstrated a significant decrease of ER ( $P < .01$ ) after injection, whereas the ERs of the STs were comparable between the two groups ( $P > .05$ ).

### Digital Microangiography

Barium suspension served as an intravascular marker or contrast agent for microangiography of the tumor vasculature. In CA4P-treated rats, unlike the opacified vasculature of laterally located STs, the HTs were hardly discernable on the whole-body microangiogram due to superimposed bony structures and extratumoral vessels (Figure 4A). However, on sectioned radiograph, intratumoral vasculature disappeared centrally from the HTs with residual vessels existing only at periphery, suggesting CA4P-induced vascular shutdown and intratumoral necrosis. STs showed both central and peripheral vessels, suggesting a lack of response to CA4P. In vehicle control rats, both HTs and STs displayed intact tumor vasculature, which though appeared much denser in HTs relative to STs (Figure 4B). Quantitatively, gray values measured on radiograph of tissue sections from HTs and STs were  $121 \pm 13.9$  and  $82.3 \pm 10.6$  in vehicle control rats and  $54.5 \pm 9.5$  and  $76.4 \pm 11.2$  in CA4P-treated rats, respectively. In vehicle control rats, vessel density of HTs was significantly higher than that of STs ( $P < .01$ ). However, vessel density of HTs in CA4P-treated group was significantly lower than that in vehicle controls ( $P < .001$ ), whereas STs from both groups were comparable in their vessel densities ( $P > .05$ ),

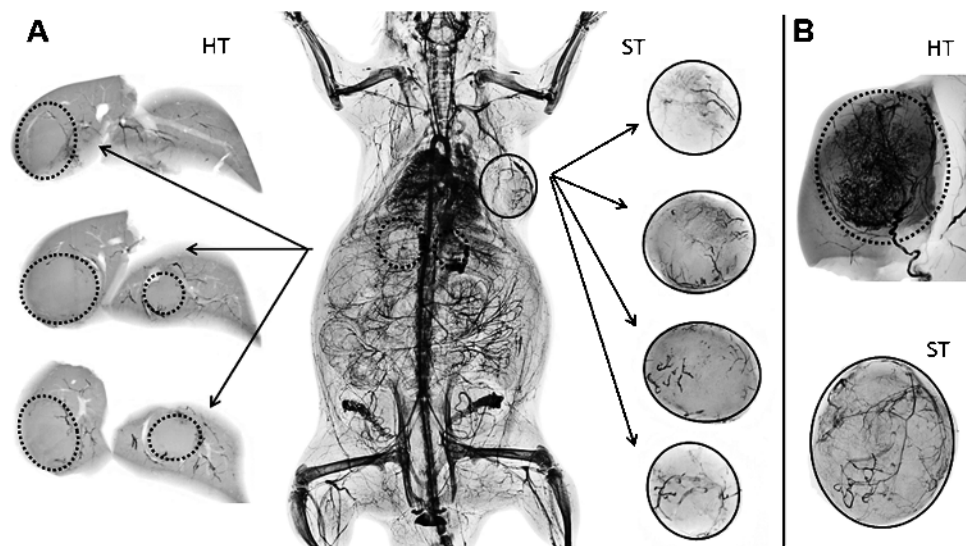


**Figure 4.** Digital microangiograms represent CA4P-treated group (A) and vehicle control group (B). (A) In CA4P-treated group, unlike the opacified vasculature of laterally located STs (solid circle), the HTs (dashed circles) were hardly discernable on the whole-body microangiogram due to superimposed bony structures and extratumoral vessels. However, on sectioned radiograph, intratumoral vasculature disappeared centrally from the HTs with residual vessels existing only at periphery, suggesting CA4P-induced vascular shutdown and intratumoral necrosis. The ST showed both central and peripheral vessels, suggesting a lack of response to CA4P, likely due to insufficient drug concentration. (B) In vehicle control rats, both HTs (dashed circles) and ST (solid circle) displayed intact tumor vasculature, though the vasculature appeared much denser in the HTs relative to ST, suggesting the richer blood supply, hence higher drug concentration, in the former than the latter.

suggesting diverse responses to CA4P between HTs and STs and consistent with the MRI and histologic findings.

#### Histologic Analysis and Correlation with MRI

Macroscopically on H&E-stained slides, intrahepatic and subcutaneous rhabdomyosarcomas (R1) both appear as spherical solid masses with clear borders to the surrounding normal tissues, but intratumoral necrosis existed only with HTs, but not with STs, after the CA4P treatment (Figure 5). Microscopically, while STs from both groups remained viable with their patent vessels filled with injected barium articles at the tumor core, HTs only from CA4P-treated group demonstrated extensive central necrosis with a few layers of viable tumor cells found adjacent to normal liver parenchyma (Figure 5). The structures of blood vessels disappeared centrally only from the CA4P-treated HTs, corresponding to a lack of central contrast enhancement on MRI (Figure 2) and a signal void from sectioned microangiography in these tumors (Figure 4). Quantitatively, for CA4P-treated HTs, tumor necrosis ratio obtained from microscopic histomorphometry ( $0.63 \pm 0.12$ ) and from CE-T1WI ( $0.59 \pm 0.13$ ) matched closely to each other ( $P > .05$ ) with a statistically significant linear correlation ( $R^2 = 0.86$ ,  $P < .001$ ) as shown in Figure 6.

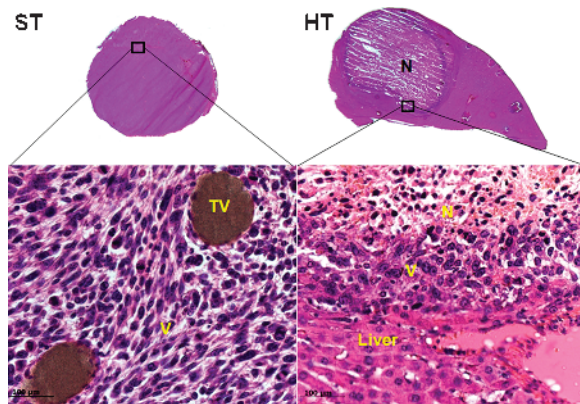


**Figure 5.** Gross and microscopic views of the H&E-stained sections of the ST and HT sections from a CA4P-treated rat. (N, tumor necrosis; TV, tumor vessel; V, viable tumor tissues). Macroscopically (upper row), both the ST (left) and HT (right) of rhabdomyosarcomas (R1) appeared as spherical solid masses with clear borders to the surrounding normal tissues. However, intratumoral necrosis existed only with the HT, but not with the ST, suggesting their diverse responses to CA4P treatment. Microscopically (lower row), the ST (left) remained viable with its intact vessels filled with injected barium articles at the tumor core. However, the HT (right) demonstrated extensive central necrosis with a few layers of viable tumor cells found adjacent to normal liver parenchyma, and the structures of blood vessels disappeared centrally, corresponding to a lack of central contrast enhancement on MRI (Figure 2) and a signal void on sectioned microangiography (Figure 4).

#### Discussion

In clinical patients, multiple growths of malignant neoplasm frequently occur due to secondary spreading from one single primary focus to elsewhere in the body. However, the majority of current studies on tumor models are done with subcutaneous models for technical simplicity. Animal models with tumors of the same origin but located in different organs or tissues are therefore mandatory to simulate the widespread metastasis in cancer patients. However, previous animal studies assessed

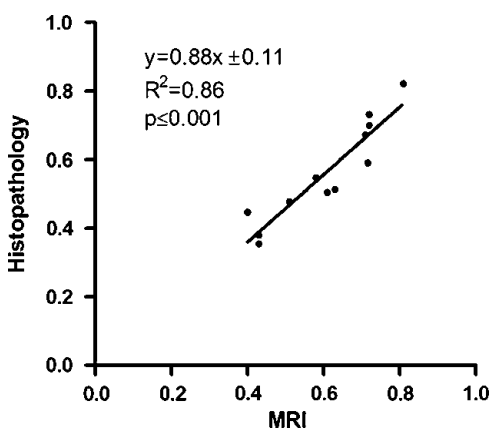


**Figure 6.** Linear correlation chart shows that tumor necrosis ratios obtained from microscopic histomorphometry and from CE-T1WI in CA4P-treated group matched closely to each other ( $P > .05$ ) with a statistically significant linear correlation ( $R^2 = 0.86$ ,  $P < .001$ ). The necrosis ratios were calculated on CE-T1WIs at 48 hours after the injection of CA4P and on postmortem H&E-stained slides on a tumor-by-tumor basis ( $n = 12$ ). The changes of necrosis ratios determined by *in vivo* MRI and *ex vivo* histopathology are negligible in all the STs.

the therapeutic responses to CA4P in either STs [34] or HTs [38] but not in both. Therefore, it was impossible to directly compare the efficacy of the same drug at a given dose in tumors of different locations. In this study, the rat model of multifocal R1 tumors allowed us to expose and document the diverse responses to CA4P in the same individual animals, which is deemed clinically relevant. This experimental setting may prove useful for screening the efficacy of other anticancer drugs or determining the adequate dosage of a certain drug in the subjects with metastatic diseases.

MRI is currently the most versatile method for noninvasive assessment of the responses to a therapy by malignant tumors [39–41]. This is realized by a comprehensive array of MRI-derived parameters as morphologic, physiological, and metabolic/molecular biomarkers for detection, characterization, and therapeutic evaluation of malignancies [13,42,43]. Besides the principal criteria of volume alteration or tumor DT as tumor growth indices for evaluating tumor response to anticancer therapies, such imaging biomarkers also include tumor necrosis ratio, ADC, and ER for quantitative assessment of tumor burden and therapeutic evaluation of tumor response after any anticancer treatment in clinical oncology trials and animal experiments [13,38,42,43].

In the present study, within 48 hours after CA4P, STs grew much faster in comparison with HTs, as reflected in the tumor volume curve and the corresponding tumor DTs. The presence and absence of necrosis in HTs and STs were evidenced by the products of necrosis ratio derived from CE-T1WIs, suggesting the diverse responses to CA4P in tumors of the same cell line but different locations. Declined ER in HTs reflected the impaired distribution of contrast agent in extravascular and intravascular space of the tumor. A close linear correlation of the necrosis ratios between CE-T1WI and the histopathology in HTs confirms the reliability of such MRI biomarkers as viability indices. ADC obtained from DWI, which defines water molecular motion in tissue and cellular environment, is elicited to characterize pathologic alterations in tumors, i.e., the changes in ADC allows for the differentiation of necrosis and edema from viable tissue [44]. Relative to the

unaltered ADC in all STs or HTs of vehicle controls, the significantly elevated ADC in HTs of CA4P-treated rats indicated an increased mobility of water molecules resulting from a decreased cellular density, disintegrated cell membrane, and loss of cell viability.

Microangiography was applied as a postmortem gold standard method to visualize and quantify tumor vascularity and CA4P-induced intratumoral vascular shutdown [13,45,46]. The barium suspension injected from the carotid artery was evenly filled in the entire arterial system covering both HTs and STs under an equal pressure, hence a more reliable comparison between tumors of different locations. In vehicle control rats, the higher and lower tumor vessel density demonstrated in HTs and STs, respectively, are understandable in view of their host organs, i.e., hypervascular liver *versus* hypovascular subcutis. Thus, HTs may be better facilitated to recruit the released angiogenic factors such as vascular endothelial growth factor, angiopoietins, and epidermal growth factor for neoangiogenic process of malignancies. Consequently, HTs with denser and immature blood vessels can be more susceptible to CA4P treatment compared to STs, as proven by the microangiographic outcomes.

The core issue related to the findings of this study is to extrapolate why HTs and STs responded differently to CA4P. It is known that response to chemotherapy is generally dose-dependent. Indeed, massive intratumoral necrosis was successfully induced in rats with STs of the same R1 cell line by CA4P at a high dose of 25 mg/kg [47], which is much higher than the maximum tolerate dose (MTD) of 68 mg/m<sup>2</sup> as defined in clinical trials of CA4P for human cancer patients [8]. The iv injected dose of CA4P at 5 mg/kg in this study is closer to the MTD in humans and therefore more clinically relevant [26]. However, this dose seems only high enough to exert tumoricidal effect on HTs but not STs, most likely due to the distinct intratumoral concentrations of the drug distributing through the vasculatures of diverse density. The exact dose to adequately cause therapeutic effect on both HTs and STs must fall into the range between 5 and 25 mg/kg and has to be further defined. Similarly, human cancers of different locations may respond also differently to CA4P at any dose lower than the MTD, which explains the overall unsatisfactory clinical outcomes despite the over 30 years' development of this drug [1]. There seems to be a justified need to redefine the best clinical dosage for CA4P that maximizes its anticancer effect but meanwhile does not render any irreversible adverse effects on cancer patients. Besides the above-mentioned vessel density-determined drug concentrations as the most straightforward explanation, other plausible reasons may include the following.

Upon iv injection, the discrepancy in responsiveness to CA4P between HTs and STs can be attributed to the differences within the inherent vessel structures, the microenvironmental components, the host-tumor interactions, and the levels of gene expression of the tumor, which may collectively affect tumor blood perfusion, diffusion, and permeability [48], resulting in reduction in blood flow and generation of hypoxia in different degrees depending on locations. Previous studies have demonstrated the presence of physiological differences in vessel density, vessel diameters, permeability, and leukocyte rolling between HTs and STs [49], which may lead to different degrees on tumor neoangiogenesis and microcirculation. Variation in heterogeneity of blood flow and vascular tortuousness within liver or STs may affect the delivery of therapeutic agents to vascular targets [13,49]. Meanwhile, dissimilar levels of gene expression have been shown in tumors of the liver and subcutaneous site, indicating the impact of microenvironment on genotypes and phenotypes of the



tumors of the same origin [50]. For instance, expressions of certain specific genes were significantly lower in HTs than in STs, whereas down-regulation of these genes was associated with the higher degree of malignancy [50]. All the above elements may lead to the more immature vasculature in HTs compared to STs, leading to distinctly higher susceptibility of HTs to CA4P, as have been demonstrated in this study.

### Study Limitations

Ktrans map was not used in this study for more robust validation of the MRI data. Ktrans map as an important index from perfusion-weighted MR image allows cross-site comparisons of hemodynamics. Characterization of hemodynamic differences between tumors of different sites may provide more valuable information for exploring the different therapeutic responses to CA4P.

To our knowledge, this study is the first time that tumors of different sites in the same animal were implanted and were gotten into the same imaging plane at approximate the same size, which allow making a striking and direct comparison between the properties of the tumors on MR images. Meanwhile, it is the first time that responses to CA4P were compared both interindividually and intra-individually in a rat model bearing both HTs and STs of the same origin. MRI and microangiography allowed quantitative documentation of the diverse therapeutic responses between tumors of different locations, which are likely caused by different drug concentrations due to distinct tumor vascularity and microenvironment. These findings emphasize the presence of cancer heterogeneity and the importance of individualization of drug delivery.

### References

- Li J, Chen F, Cona MM, Feng Y, Himmelreich U, Oyen R, Verbruggen A, and Ni Y (2012). A review on various targeted anticancer therapies. *Target Oncol* 7, 69–85.
- Schnitzer JE (1998). Vascular targeting as a strategy for cancer therapy. *N Engl J Med* 339, 472–474.
- Arap W, Pasqualini R, and Ruoslahti E (1998). Cancer treatment by targeted drug delivery to tumor vasculature in a mouse model. *Science* 279, 377–380.
- Ching LM, Zwain S, and Baguley BC (2004). Relationship between tumour endothelial cell apoptosis and tumour blood flow shutdown following treatment with the antivascular agent DMXAA in mice. *Br J Cancer* 90, 906–910.
- Seshadri M, Spornyak JA, Maiery PG, Cheney RT, Mazurchuk R, and Bellnier DA (2007). Visualizing the acute effects of vascular-targeted therapy *in vivo* using intravital microscopy and magnetic resonance imaging: correlation with endothelial apoptosis, cytokine induction, and treatment outcome. *Neoplasia* 9, 128–135.
- McPhail LD, McIntyre DJ, Ludwig C, Kestell P, Griffiths JR, Kelland LR, and Robinson SP (2006). Rat tumor response to the vascular-disrupting agent 5,6-dimethylxanthene-4-acetic acid as measured by dynamic contrast-enhanced magnetic resonance imaging, plasma 5-hydroxyindoleacetic acid levels, and tumor necrosis. *Neoplasia* 8, 199–206.
- Ching L, Goldsmith D, Joseph WR, Korner H, Sedgwick JD, and Baguley BC (1999). Induction of intratumoral tumor necrosis factor (TNF) synthesis and hemorrhagic necrosis by 5,6-dimethylxanthene-4-acetic acid (DMXAA) in TNF knockout mice. *Cancer Res* 59, 3304–3307.
- Rustin GJ, Galbraith SM, Anderson H, Stratford M, Folkes LK, Sena L, Gumbrell L, and Price PM (2003). Phase I clinical trial of weekly combretastatin A4 phosphate: clinical and pharmacokinetic results. *J Clin Oncol* 21, 2815–2822.
- Tozer GM, Kanthou C, and Baguley BC (2005). Disrupting tumour blood vessels. *Nat Rev Cancer* 5, 423–435.
- Rustin MZaG (2010). The clinical development of tubulin binding vascular disrupting agents. In *Vascular Disruptive Agents for the Treatment of Cancer*. T Meyer (Ed.). Springer. pp. 183–216: Part 3.
- Li J, Raymond O, Verbruggen A, and Ni Y (in press). Small molecule sequential dual-targeting theragnostic strategy (SMSDTTS): from preclinical experiments towards possible clinical anticancer applications. *J Cancer*.
- Cooney MM, Ortiz J, Bukowski RM, and Remick SC (2005). Novel vascular targeting/disrupting agents: combretastatin A4 phosphate and related compounds. *Curr Oncol Rep* 7, 90–95.
- Wang H, Sun X, Chen F, De Keyzer F, Yu J, Landuyt W, Vandecaveye V, Peeters R, Bosmans H, Hermans R, et al. (2009). Treatment of rodent liver tumor with combretastatin a4 phosphate: noninvasive therapeutic evaluation using multiparametric magnetic resonance imaging in correlation with microangiography and histology. *Invest Radiol* 44, 44–53.
- Anderson HL, Yap JT, Miller MP, Robbins A, Jones T, and Price PM (2003). Assessment of pharmacodynamic vascular response in a phase I trial of combretastatin A4 phosphate. *J Clin Oncol* 21, 2823–2830.
- Zweifel M, Jayson GC, Reed NS, Osborne R, Hassan B, Ledermann J, Shreeves G, Poupard L, Lu SP, Balkissoon J, et al. (2011). Phase II trial of combretastatin A4 phosphate, carboplatin, and paclitaxel in patients with platinum-resistant ovarian cancer. *Ann Oncol* 22, 2036–2041.
- West CM and Price P (2004). Combretastatin A4 phosphate. *Anticancer Drugs* 15, 179–187.
- Tozer GM, Prise VE, Wilson J, Cemazar M, Shan S, Dewhirst MW, Barber PR, Vojnovic B, and Chaplin DJ (2001). Mechanisms associated with tumor vascular shut-down induced by combretastatin A-4 phosphate: intravital microscopy and measurement of vascular permeability. *Cancer Res* 61, 6413–6422.
- Tozer GM, Prise VE, Lewis G, Xie S, Wilson I, and Hill SA (2009). Nitric oxide synthase inhibition enhances the tumor vascular-damaging effects of combretastatin a-4 3-o-phosphate at clinically relevant doses. *Clin Cancer Res* 15, 3781–3790.
- Salmon BA and Siemann DW (2007). Characterizing the tumor response to treatment with combretastatin A4 phosphate. *Int J Radiat Oncol Biol Phys* 68, 211–217.
- Li J, Sun Z, Zhang J, Shao H, Miranda Cona M, Wang H, Marysael T, Chen F, Prinsen K, Zhou L, et al. (2011). A dual-targeting anticancer approach: soil and seed principle. *Radiology* 260, 799–807.
- Rustin GJ, Shreeves G, Nathan PD, Gaya A, Ganesan TS, Wang D, Boxall J, Poupard L, Chaplin DJ, Stratford MR, et al. (2010). A phase Ib trial of CA4P (combretastatin A-4 phosphate), carboplatin, and paclitaxel in patients with advanced cancer. *Br J Cancer* 102, 1355–1360.
- Mitrus I, Sochanik A, Cichon T, and Szala S (2009). Combination of combretastatin A4 phosphate and doxorubicin-containing liposomes affects growth of B16-F10 tumors. *Acta Biochim Pol* 56, 161–165.
- Bilenker JH, Flaherty KT, Rosen M, Davis L, Gallagher M, Stevenson JP, Sun W, Vaughn D, Giantonio B, Zimmer R, et al. (2005). Phase I trial of combretastatin a-4 phosphate with carboplatin. *Clin Cancer Res* 11, 1527–1533.
- Chen F, Feng Y, Zheng K, De Keyzer F, Li J, Feng Y, Miranda CM, Wang H, Jiang Y, Yu J, et al. (2012). Enhanced antitumor efficacy of a vascular disrupting agent combined with an antiangiogenic in a rat liver tumor model evaluated by multiparametric MRI. *PLoS One* 7, e41140.
- Tozer GM, Kanthou C, Lewis G, Prise VE, Vojnovic B, and Hill SA (2008). Tumour vascular disrupting agents: combating treatment resistance. *Br J Radiol* 81, S12–S20.
- Prise VE, Honess DJ, Stratford MR, Wilson J, and Tozer GM (2002). The vascular response of tumor and normal tissues in the rat to the vascular targeting agent, combretastatin A-4-phosphate, at clinically relevant doses. *Int J Oncol* 21, 717–726.
- Gridelli C, Rossi A, Maione P, Rossi E, Castaldo V, Sacco PC, and Colantuoni G (2009). Vascular disrupting agents: a novel mechanism of action in the battle against non-small cell lung cancer. *Oncologist* 14, 612–620.
- Siemann DW and Horsman MR (2009). Vascular targeted therapies in oncology. *Cell Tissue Res* 335, 241–248.
- Wang H, Cona MM, Chen F, Yu J, Feng Y, Li J, Keyzer FD, Marchal G, and Ni Y (2012). Comparison of two vascular-disrupting agents at a clinically relevant dose in rodent liver tumors with multiparametric magnetic resonance imaging biomarkers. *Anticancer Drugs* 23, 12–21.
- Wang H, Marchal G, and Ni Y (2011). Multiparametric MRI biomarkers for measuring vascular disrupting effect on cancer. *World J Radiol* 3, 1–16.
- Chen F, De Keyzer F, and Ni Y (2011). Cancer models—multiparametric applications of clinical MRI in rodent hepatic tumor model. *Methods Mol Biol* 771, 489–507.



- [32] Evelhoch JL, LoRusso PM, He Z, DelProposto Z, Polin L, Corbett TH, Langmuir P, Wheeler C, Stone A, Leadbetter J, et al. (2004). Magnetic resonance imaging measurements of the response of murine and human tumors to the vascular-targeting agent ZD6126. *Clin Cancer Res* **10**, 3650–3657.
- [33] Vogel-Claussen J, Gimi B, Artemov D, and Bhujwalla ZM (2007). Diffusion-weighted and macromolecular contrast enhanced MRI of tumor response to antivascular therapy with ZD6126. *Cancer Biol Ther* **6**, 1469–1475.
- [34] Thoeny HC, De Keyzer F, Vandecaveye V, Chen F, Sun X, Bosmans H, Hermans R, Verbeken EK, Boesch C, Marchal G, et al. (2005). Effect of vascular targeting agent in rat tumor model: dynamic contrast-enhanced versus diffusion-weighted MR imaging. *Radiology* **237**, 492–499.
- [35] Chen F, Sun X, De Keyzer F, Yu J, Peeters R, Coudyzer W, Vandecaveye V, Landuyt W, Bosmans H, Van Hecke P, et al. (2006). Liver tumor model with implanted rhabdomyosarcoma in rats: MR imaging, microangiography, and histopathologic analysis. *Radiology* **239**, 554–562.
- [36] Schwartz M (1961). A biomathematical approach to clinical tumor growth. *Cancer* **14**, 1272–1294.
- [37] Sun X, Wang H, Chen F, De Keyzer F, Yu J, Jiang Y, Feng Y, Li J, Marchal G, and Ni Y (2009). Diffusion-weighted MRI of hepatic tumor in rats: comparison between *in vivo* and postmortem imaging acquisitions. *J Magn Reson Imaging* **29**, 621–628.
- [38] Wang H, Li J, Chen F, De Keyzer F, Yu J, Feng Y, Nuyts J, Marchal G, and Ni Y (2010). Morphological, functional and metabolic imaging biomarkers: assessment of vascular-disrupting effect on rodent liver tumours. *Eur Radiol* **20**, 2013–2026.
- [39] Therasse P, Arbuck SG, Eisenhauer EA, Wanders J, Kaplan RS, Rubinstein L, Verweij J, Van Glabbeke M, van Oosterom AT, Christian MC, et al. (2000). New guidelines to evaluate the response to treatment in solid tumors. *J Natl Cancer Inst* **92**, 205–216.
- [40] Husband JE, Schwartz LH, Spencer J, Ollivier L, King DM, Johnson R, and Reznick R (2004). Evaluation of the response to treatment of solid tumours—a consensus statement of the International Cancer Imaging Society. *Br J Cancer* **90**, 2256–2260.
- [41] Ollivier L, Leclerc J, Thiesse P, Di Stefano D, and Vincent C (2007). Measurement of tumour response to cancer treatment: morphologic imaging role. *Bull Cancer* **94**, 171–177.
- [42] Padhani AR and Miles KA (2010). Multiparametric imaging of tumor response to therapy. *Radiology* **256**, 348–364.
- [43] Tozer GM (2003). Measuring tumour vascular response to antivascular and antiangiogenic drugs. *Br J Radiol* **76**, S23–S35.
- [44] Colvin DC, Jourquin J, Xu J, Does MD, Estrada L, and Gore JC (2011). Effects of intracellular organelles on the apparent diffusion coefficient of water molecules in cultured human embryonic kidney cells. *Magn Reson Med* **65**, 796–801.
- [45] Wu X, Wang H, Chen F, Jin L, Li J, Feng Y, DeKeyzer F, Yu J, Marchal G, and Ni Y (2009). Rat model of reperfused partial liver infarction: characterization with multiparametric magnetic resonance imaging, microangiography, and histomorphology. *Acta Radiol* **50**, 276–287.
- [46] Ni Y, Marchal G, van Damme B, van Hecke P, Michiels J, Zhang X, Yu J, and Baert AL (1992). Magnetic resonance imaging, microangiography, and histology in a rat model of primary liver cancer. *Invest Radiol* **27**, 689–697.
- [47] Thoeny HC, De Keyzer F, Chen F, Ni Y, Landuyt W, Verbeken EK, Bosmans H, Marchal G, and Hermans R (2005). Diffusion-weighted MR imaging in monitoring the effect of a vascular targeting agent on rhabdomyosarcoma in rats. *Radiology* **234**, 756–764.
- [48] Wang ES, Pili R, and Seshadri M (2012). Modulation of chemotherapeutic efficacy by vascular disrupting agents: optimizing the sequence and schedule. *J Clin Oncol* **30**, 760–761.
- [49] Fukumura D, Yuan F, Monsky WL, Chen Y, and Jain RK (1997). Effect of host microenvironment on the microcirculation of human colon adenocarcinoma. *Am J Pathol* **151**, 679–688.
- [50] Ohta S, Lai EW, Morris JC, Pang AL, Watanabe M, Yazawa H, Zhang R, Green JE, Chan WY, Sirajuddin P, et al. (2008). Metastasis-associated gene expression profile of liver and subcutaneous lesions derived from mouse pheochromocytoma cells. *Mol Carcinog* **47**, 245–251.